Synthesis and Physical Characterization of Thermoelectric Single Crystals

by

Juan Pablo Porras Pérez Guerrero

Submitted to the Department of Physics
in partial fulfillment of the requirements for the Degree of

BACHELOR OF SCIENCE

at the

MASSACHUSETTS INSTITUTE OF TECHNOLOGY

June, 2012

Signature of Author .....
Department of Physics
May 11, 2012

Certified by.....
Young S. Lee
Thesis Supervisor, Department of Physics

Accepted by .....
Professor Nergis Mavalvala
Senior Thesis Coordinator, Department of Physics

Synthesis and Physical Characterization of Thermoelectric Single Crystals

by

Juan Pablo Porras Pérez Guerrero

Submitted to the Department of Physics
on May 11, 2012, in partial fulfillment of the
requirements for the Degree of
BACHELOR OF SCIENCE

Abstract

There is much current interest in thermoelectric devices for sustainable energy. This thesis describes a research project on the synthesis and physical characterization of thermoelectric single crystals. $In_4Se_{3-\delta}$ crystals were grown by different methods including the use of a floating zone furnace and a three-zone furnace, as well as different initial compositions. The samples obtained each time, either crystalline or powder, were analyzed using x-ray diffraction to find the phases present, and orientations in the case of crystals. The crystals were studied by the means of neutron scattering at Oak Ridge National Laboratory, and the results presented differences from previous literature reports and a non-zero intensity of forbidden Bragg peaks was noted. Simulations of the effect of Se vacancies in the crystal were executed to explore this last phenomenon. Measurements of the electrical resistivity ρ and Seebeck coefficient S of the crystal related to the figure of merit $ZT = \frac{S^2T}{\rho\kappa}$ were compared with the values presented by other groups.

Thesis Supervisor: Young S. Lee

Acknowledgments

Juan P. Porras gratefully acknowledges Professor Young S. Lee for his supervision, input and support throughout this project. The author also thanks Dillon Gardner, Scott Speakman, Shaoyan Chu, Anna Y. Ho and everyone in the Lee group for their help and input.

Contents

List of Figures

List of Tables

Chapter 1

Introduction

With the current interest in sustainable sources of energy, thermoelectric materials have been of great interest due to their ability to convert waste heat into electricity, and because of the emergence of clean cooling technologies that use these materials. The figure of merit ZT, which is proportional to the electrical conductivity and inversely proportional to the thermal conductivity, characterizes the performance of such materials. In order to improve performance, attempts to reduce the thermal conductivity of phonons, while preserving electric conductivity, are pursued.

This thesis describes the research project on the synthesis and physical characterization of thermoelectric single crystals. The material of interest is In_4Se_3 , which is an n-type thermoelectric. Some background on thermoelectric materials is described in Chapter 2, where the efficiency as a function of the figure of merit ZT is derived.

The properties of In_4Se_3 crystals are described in Chapter 3. The structure of the In_4Se_3 is such that strongly bound chains of atoms form along one direction, which are weakly bound to other chains. Previous experiments propose that a Peierls distortion along these chains causes the material to have good electrical conductivity while keeping a low thermal conductivity. Such a distortion would cause a superlattice structure to appear. One of the initial objectives of the project was to characterize the superlattice structure.

Chapter 4 introduces the techniques used to grow the crystals. A peritectic point in the phase diagram of In-Se makes it difficult to synthesize single crystals. Start-

ing from elemental indium and selenium, the crystals were grown by the Bridgman method in three different setups.

The theory of wave diffraction by crystals is necessary to understand x-ray diffraction and neutron scattering experiments, and is introduced in Chapter 5. The Bragg condition is derived from geometrical considerations, and a formula for the scattering amplitude as a function of the structure factor and the atomic form factor is obtained.

Chapter 6 details the x-ray diffraction experiments. Phase identification and phase quantization were performed on powder samples using x-ray diffraction to verify the growth process. Single crystal diffraction was used to determine the orientation of the crystals to be used in neutron scattering.

A neutron scattering experiment was carried out to examine the structure of the crystals, and is described in Chapter 7. An attempt to characterize the superlattice structure using elastic neutron scattering was made. The phonon dispersion was intended to be studied by inelastic neutron scattering. These measurements proved difficult due to small scattered signal. However, two interesting observations were made: a non-zero intensity of forbidden Bragg peaks, and a difference in intensity between (h, k, l) and $(\bar{h}, \bar{k}, \bar{l})$ peaks.

To study the non-zero intensity of forbidden peaks, the effect of selenium vacancies was evaluated using simulations as described in Chapter 8. The results of the measurements of the thermoelectric properties and the conclusions drawn out are outlined in Chapter 9.

Chapter 2

Thermoelectric devices

A thermoelectric device is capable of directly converting thermal energy into electricity, or creating a temperature difference when current is applied. Thermoelectric devices have a few advantages over other conversion systems, for example that they require only solid-state components for the conversion and no moving parts. Therefore they are reliable, compact and noise-free. However the cost and efficiency of current devices are such that applications are limited. Thermoelectric generators in conjunction with a radioactive source are used in space to power satellites and probes, where other means of energy are unavailable. Refrigerators are used in coolers where portability is necessary and the loads are small. In recent years, thermoelectric materials have been of great interest for sustainable energy applications. The potential to convert waste heat to electricity that these materials hold, or the clean cooling technologies that they promise is very attractive.

This chapter deals with the conversion of heat to electricity in a semi-conductor by the means of the Seebeck effect, and the use of a thermoelectric for refrigeration by the means of the Peltier effect. The third thermoelectric effect, the Thomson effect, will not be treated in this chapter.

The Seebeck effect was first observed by Thomas Seebeck in 1823[1]. Suppose that a rod of material, has the temperature set to T at its center, $T + \frac{\Delta T}{2}$ at one end and $T - \frac{\Delta T}{2}$ at the other. Then the voltage measured between the ends is related to

the temperature difference by

$$\Delta V = S(T)\Delta T, \tag{2.1}$$

where $S(T)$ is the Seebeck coefficient at temperature T for the material in question. The Seebeck effect is therefore a way to use a temperature difference to supply a voltage.

The Peltier effect discovered by Jean-Charles Peltier in 1834[2], is the effect by which a flow of current I through a material causes a flow of heat $\dot{Q}$ such that

$$\dot{Q} = \frac{\mathrm{d}\,Q}{\mathrm{d}\,T} = \Pi(T)I, \tag{2.2}$$

where $\Pi(T)$ is the Peltier coefficient at temperature T, and it is related to S by $\Pi(T) = TS(T)$.

2.1 Device overview

A generic thermoelectric device is shown in Figure 2-1. Notice that the thermoelectric effect occurs in the thermoelements: the n-type material carries electrons in the same direction as the heat flow, hence current is opposite to heat flow. On the other hand the p-type material carries holes in the direction of the heat flow, hence current is in the same direction as heat flow. In other words the Seebeck coefficients are such that $S_n < 0$ and $S_p > 0$. By connecting these two types of materials we get a circuit, where current flows from E_n to n to R to p to E_p, as labeled in Figure 2-1, and heat flows from R to E_n and E_p. Therefore the two thermoelements are electrically in series and thermally in parallel.

When the device is used as a generator, the circuit is closed by connecting E_n and E_p to an electrical load R_{load}. The heat source supplies heat to the conducting plate R. Then electrons in R are thermally excited to above the Fermi energy, and may move to the conduction band of the n-type material, where they are free to move to the conducting plate E_n and release the extra heat to the heat sink. Holes left by electrons can be thought of as positively charged and traveling in the opposite

direction to electrons, through the p-type material and into the conducting plate labeled E_p. Figure 2-2 is a band diagram where the paths taken by electrons and holes respectively is shown. The slope of the the energy gap in the thermoelements represents the effect of Joule heating, treated in Section 2.2.

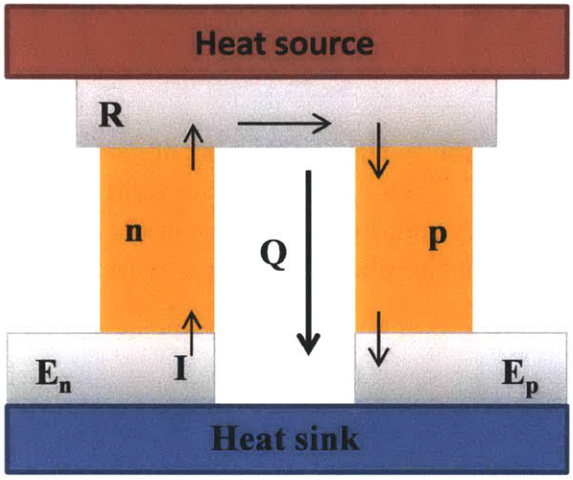

Figure 2-1: Schematic of a thermoelectric device. R, E_n and E_p represent conducting plates, n and p label the n-type and p-type thermoelements. The directions of the heat Q and current I are indicated by arrows.

In a refrigerator, a current is supplied at E_n and goes through the device, allowing heat to be transferred from R to E_n and E_p by the same process as before; the net effect of applying a current is therefore cooling the load and heating the sink. Note that heat conduction in the opposite direction may not occur in the ideal case, when heat conduction is only mediated by charge carriers, even though the temperature is generally higher in the sink than in the load.

2.2 Efficiency and irreversiblities

In this section only the case of a thermoelectric generator is considered, but the analysis for a refrigerator is completely analogous. The derivation is based on [3]; additional information can be found in [4].

For an ideal generator, the first and second laws of thermodynamics for a cycle can be written as

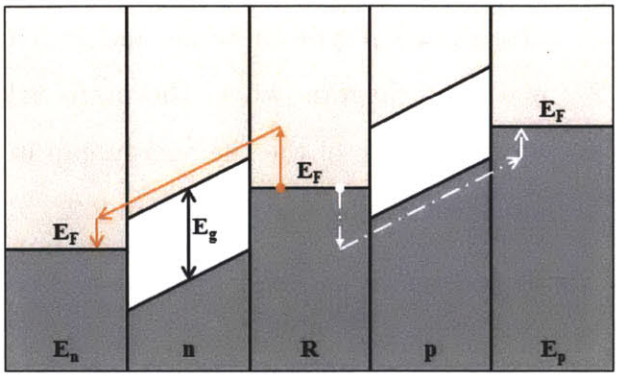

Figure 2-2: Band diagram for a thermoelectric device. The different components are labeled as in Figure 2-1. Electrons follow the solid arrows and holes the dashed arrows. E_g denotes the energy band gap, and the energy scale is $k_B T$ where k_B is the Boltzmann constant and T is the absolute temperature.

$$\Delta U = Q_{in} - Q_{out} - W = 0\,, \tag{2.3a}$$

$$\Delta S = \frac{Q_{in}}{T_h} - \frac{Q_{out}}{T_c} = 0\,. \tag{2.3b}$$

where W is the work done by the generator, Q_{in} is the heat going into the system through R at $T = T_h$ and Q_{out} is the heat leaving the system through E_n and E_p at $T = T_c$. Combining the equations 2.3a and 2.3b, an expression for the Carnot limit to efficiency results

$$\eta_c = \frac{W}{Q_{in}} = 1 - \frac{T_c}{T_h} = \frac{\Delta T}{T_h}, \tag{2.4}$$

The power generated is $\dot{W} = IV$, where I is the current through the circuit, and V denotes the voltage between E_n and E_p due to the Seebeck effect. Using equation 2.1, the power can be written as

$$\dot{W} = I(S_p - S_n)\Delta T = I S_m \Delta T, \tag{2.5}$$

and the heat transfer rate $\dot{Q}$, as

$$\dot{Q} = \frac{\dot{W}}{\eta_c} = I S_m T_h. \tag{2.6}$$

Nevertheless two main irreversibilities must be considered in the system for a real

device: Joule heating and thermal diffusion in the thermoelectric materials. Joule heating is the loss of energy of the electrons to the crystal lattice, that is characterized macroscopically by the electrical resistance of the material R_m. Thermal diffusion inside the material can be thought of as the transport of heat by phonons instead of electrons and is characterized by the thermal conductivity of the material K_m. For the current analysis the electrical resistance of the conducting plates R, E_n and E_p is neglected.

The voltage is reduced by the non-zero resistance of the thermoelements, so the electrical power is now written as

$$\dot{W} = IV = IS_m\Delta T - I^2(R_n + R_p) = IS_m\Delta T - I^2R_m, \tag{2.7}$$

where R_n and R_p are the electrical resistances of the thermoelements. Note that resistances in series add directly.

In a similar manner the heat needed to produce a given voltage increases due to thermal losses, but decreases due to Joule heating. Approximately half of the heat due to Joule heating goes into R and half into E_n and E_p, so the heat transfer rate into the system is

$$\dot{Q} = IS_mT_h + (K_n + K_p)\Delta T - \frac{I^2R_m}{2} = IS_mT_h + K_m\Delta T - \frac{I^2R_m}{2}. \tag{2.8}$$

where K_n and K_p are the thermal conductances of the thermoelements. Note that conductances in parallel add directly.

Finally the efficiency becomes

$$\eta = \frac{IS_m\Delta T - I^2R_m}{IS_mT_h + K_m\Delta T - \frac{I^2R_m}{2}} \tag{2.9}$$

This equation can be non-dimensionalized by choosing $\lambda = \frac{IS_m}{K_m}$, $\gamma = Z\Delta T$, $\alpha =$

$Z\bar{T} = Z\frac{T_h+T_c}{2}$ and $Z = \frac{S_m^2}{K_m R_m}$. Then equation 2.9 becomes

$$\eta = 1 - \frac{\lambda\alpha + \gamma - \frac{1}{2}(\lambda\gamma - \lambda^2)}{\lambda\alpha + \gamma + \frac{1}{2}(\lambda\gamma - \lambda^2)}. \tag{2.10}$$

Taking the derivative with respect to λ and setting it to zero to maximize efficiency gives $\lambda_{max} = \frac{\gamma}{\alpha}(\sqrt{1+\alpha}-1)$. In practice this is achieved by taking $R_{load} = \sqrt{1+\alpha}R_m$. Plugging λ_{max} into the equation for η yields

$$\eta = \eta_c \left(\frac{\sqrt{1+Z\bar{T}} - 1}{\sqrt{1+Z\bar{T}} + 1 - \eta_c} \right). \tag{2.11}$$

This final result depends only on the thermodynamic limit η_c and $Z\bar{T}$, where Z is called the thermoelectric figure of merit, and encapsulates the relevant properties of the material. In the case where the thermoelements have similar properties (i.e $S = -S_n = S_p$, $R = R_n = R_p$ and $K = K_m = K_p$), then Z simplifies to $Z = \frac{S}{KR}$. Additionally if they have uniform cross sectional area A and length L, then $R = \rho\frac{L}{A}$ and $K = \kappa\frac{A}{L}$, therefore

$$Z = \frac{S^2}{\rho\kappa}, \tag{2.12}$$

where Z depends only on intrinsic quantities ρ the electrical resistivity and κ the thermal conductivity. For most thermoelectric materials currently used, $Z\bar{T} \approx 1$. For a given heat source at $T_h = 600$K and $\Delta T = 300$K, then $\eta_c = 0.5$ and the efficiency is $\eta = 0.11$, which is small compared to conventional engines with efficiencies ranging from 0.2 to 0.4. For thermoelectrics to be competitive for power generation $Z\bar{T}$ most be at least 3. That is why the study of materials such as In_4Se_3 with figure of merits exceeding 1 is of great importance.

Chapter 3

Properties of In_4Se_3 crystals

3.1 General properties

In_4Se_3 is composed of indium (In) with atomic number $Z_{In} = 49$ and selenium (Se) with $Z_{Se} = 34$ bonded by ionic-covalent interactions. It is a semiconductor with an energy bandgap around 0.65eV[5], and has a negative Seebeck coefficient; a high value of $ZT = 1.48$ has been achieved in this material[6]. Therefore this material constitutes a good candidate for a n-type thermoelectric.

The crystal structure is orthorhombic, and belongs to the Pnnm space group. The lattice vectors have magnitude $a = 15.296\mathring{A}$, $b = 12.308\mathring{A}$ and $c = 4.0806\mathring{A}$[7]. The unit cell is composed of 28 atoms: 16 In and 12 Se. The positions of the 7 irreducible

Table 3.1: Position of irreducible atoms in In_4Se_3 unit cell specified using the lattice coordinate system. Adapted from [7]

Index	Atom	Coordinates		
1	In1	0.71105	0.33933	0
2	In2	0.81578	0.52362	0
3	In3	0.96733	0.64423	0
4	In4	0.42369	0.39749	0
5	Se1	0.90329	0.84943	0
6	Se2	0.76875	0.13857	0
7	Se3	0.42410	0.15595	0

atoms are indicated in Table 3.1[7]. The positions of all the atoms in the unit cell were calculated using the Balls & Sticks software[8] by applying the imposed symmetry operations of the space group. Table A.1 in the Appendix A contains the results. A diagram of the crystal structure of the unit cell is shown in Figure 3-1.

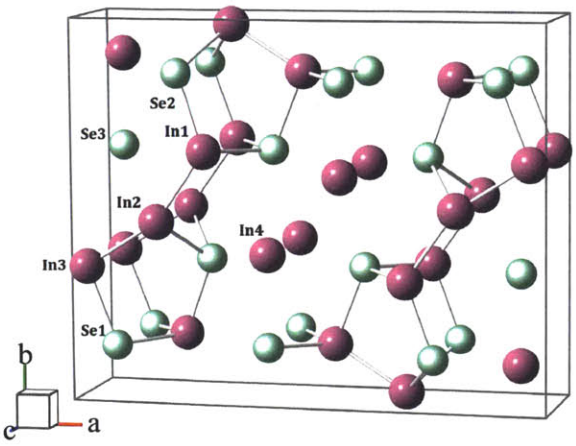

Figure 3-1: Crystal structure of the unit cell of In_4Se_3 . Perspective view of the a-b plane. In are depicted in purple, Se in green.[8]

In_4Se_3 can be described as having mixed valency $In_4Se_3 = [In]^+ \left[(In_3)^{5+}\right] \left[Se^{2-}\right]_3$. This gives rise to a chained structure where the $\left[(In_3)^{5+}\right]$, labeled In1, In2 and In3, forms ionic-covalent bonds with the $\left[Se^{2-}\right]$ to form a cluster as seen in Figure 3-1. $[In]^+$, labeled In4, interacts with the clusters more weakly through covalent bonds. This results in chains along the b-direction, coupled in the a-direction through van der Waals interactions as depicted in Figure 3-3.

3.2 Peierls distortion in $In_4Se_{3-\delta}$

Due to the presence of these chains the material has anisotropic thermoelectric properties, with the b-direction being the direction of interest, since both electrical resistivity ρ and thermal conductivity κ are relatively small in that direction. In recent work by Rhyee and coworkers[6], it is proposed that $In_4Se_{3-\delta}$ crystals can achieve a high value for the figure of merit ZT due to lattice distortions along the chain direction. The authors suggest that the nesting of the Fermi surface in this material due to the

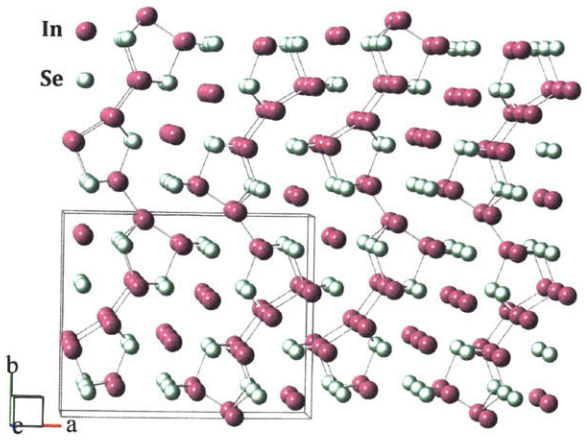

Figure 3-2: Chain structure of In_4Se_3 crystals. Perspective view of the a-b plane.[8]

change in composition δ causes a charge-density wave (CDW) instability to appear, as indicated by their electron susceptibility χ calculations and the high-resolution transmission electron microscopy (HRTEM) measurements of their crystals. They show that for the symmetry line $X(0, 1/2, 0) - U(0, 1/2, 1/2)$, χ has a singularity at the $(h, k, l) = (0, 1/2, 1/16)$ point, which corresponds to superlattice peaks in the HRTEM measurements.

One of the focuses of the project described in this work was to find and characterize the superlattice structure of $In_4Se_{3-\delta}$ crystals. A distortion in a 1-D chain effectively changes the lattice constant as depicted in Figure 3-3, thus giving rise to a super-structure at fractional values of the original lattice. The neutron scattering experiment described in Chapter 7 aims to measure the scattering from superlattice peaks to compare with the previous results.

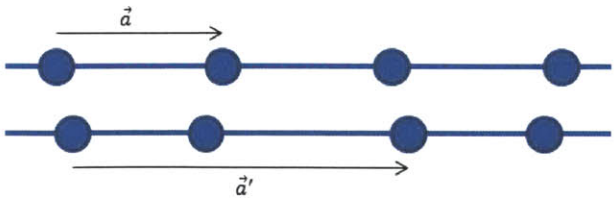

Figure 3-3: Peierls distortion of a 1-D chain. An undistorted chain with lattice vector $\vec{a}$ (top), the distorted chain with different lattice vector (bottom). The distortion was chosen to be along the direction of the chain for the schematic, but transversal distortions are also possible.

Chapter 4

Growth of In_4Se_3 crystals

This chapter presents the techniques used in crystal growth of In_4Se_3 , different methods were tried including the use of a floating zone furnace, a three zone furnace, and a box furnace adapted to have a vertical temperature gradient, along with different initial compositions. The growth techniques used are based on the Bridgman-Stockbarger technique.

The Bridgman-Stockbarger technique is a technique for crystal growth where the material is heated above its melting temperature and slowly cooled from one end of the container, where a seed is located. A single crystal with the same orientation as the seed is grown as different parts of the container are cooled below the melting temperature. The difference between Bridgman and Stockbarger is that in the Bridgman method the container is stationary and the temperature is changed whereas for Stockbarger the container is pulled from a hot region to a cold region.

The phase diagram for In-Se is presented in Figure 4-1. It is of interest to note that the In_4Se_3 phase (42% composition) rests below a region of mixed phases L+InSe 3R, so the melting of In_4Se_3 is incongruent. The other feature to point out is the monotectic point at 33% composition indium where the liquid phase goes to In_4Se_3 and liquid In. These two different compositions were used to obtain In_4Se_3 . The melting point of In_4Se_3 will be labeled hereafter as $T_m = 550°C$, and the temperature at which a 33% liquid solidifies as $T_{33} = 520°C$.

The samples are prepared in the laboratory, starting from pure indium and se-

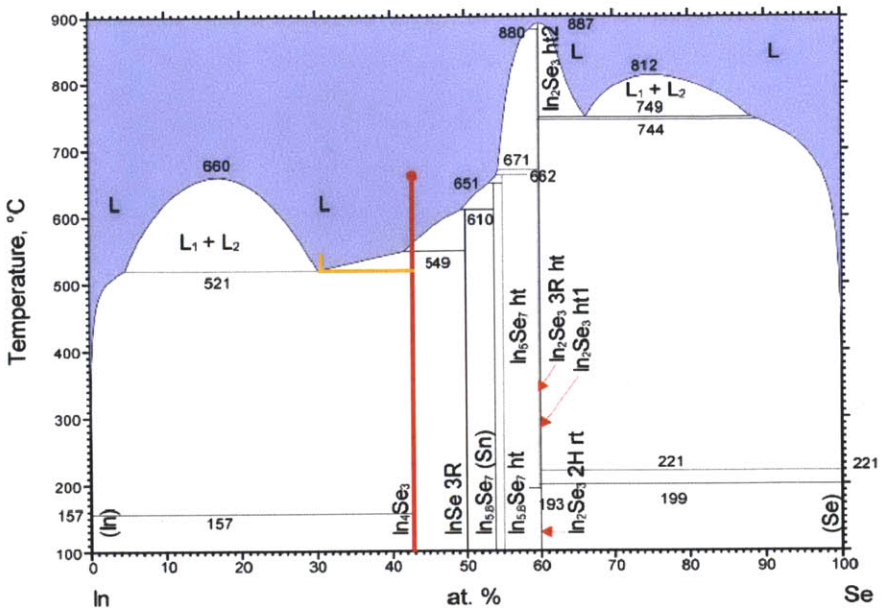

Figure 4-1: In-Se binary phase diagram, adapted from [9]. The red line indicates the path taken when starting with stoichiometric composition, the orange line when using the 33% composition.

lenium in metal form. For each sample, the pellets are weighed using an analytical balance, and sealed in a quartz tube under vacuum. After each growth, the phases are analyzed using x-ray diffraction (XRD) described in Chapter 6.

4.1 First growth

The first attempt consists of taking samples with stoichiometric composition, heating them to 750°C in a box furnace as depicted in Figure 4-2, and then cooling them down slowly at a rate of $r = -0.1$°C/min.

This method proved ineffective since the resulting solid had three phases: InSe,In_4Se_3 and In, furthermore InSe accounted for up to 75% of the sample. This result can be explained from the incongruent melting of In_4Se_3 as mentioned before. While the temperature is above T_m and below 580°C, InSe precipitates in the sample, and the composition moves towards the peritectic point. If complete equilibrium could be achieved at T_m then the InSe would react with the liquid to form only In_4Se_3 . In fact In_4Se_3 is formed at the interface causing the reaction to stop or proceed very slowly,

and the final sample has a considerable amount of InSe.

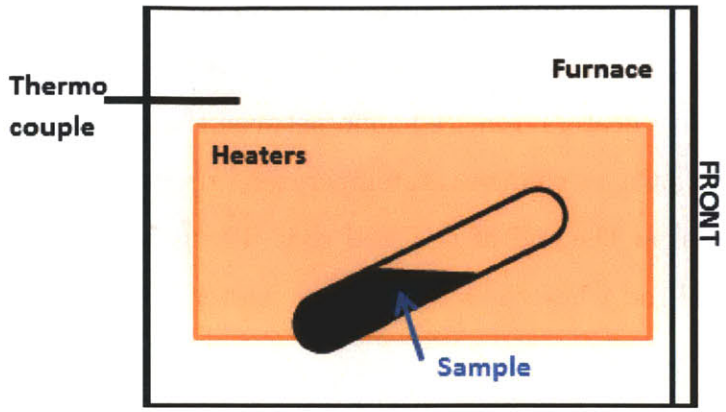

Figure 4-2: Side-view diagram of the box furnace used for growth. The heaters are located on each side of the sample, the thermocouple measures the temperature at the middle of the back. An angle is imposed on the tube to get more compact samples.

4.2 Quenching method

To avoid the formation of InSe, a second approach is considered. A sample with stoichiometric composition is heated to 950°C in the box furnace and quenched in room temperature water, then is ground into a powder. The powder is annealed at 530°C for several days and then ground again.

This method is appropriate for obtaining In_4Se_3 powder or polycrystalline samples, but no single crystals can be obtained by this approach, since multiple domains solidify into In_4Se_3 at the same time and temperature.

This method is also used to get 33% composition samples where the powder is mixed at the desired ratio for the following growths.

4.3 Floating zone furnace

The next step aims to produce single crystals from the powder obtained by quenching, by using a floating zone furnace. Powder with the stoichiometric composition is pressed into a rod, to be used as a seed, whereas powder with the 33% composition is made into a feed rod.

A growth in a floating zone furnace is done inside an evacuated quartz cylinder, the seed rod is set on the bottom and the feed rod is set on the top as depicted in Figure 4-3, and is set to rotate around its axis. By moving the rods closer to the focus point of the radiative heaters a melted zone between the rods is achieved. The rods are slowly moved down to change the temperature gradient in the material, which crystallizes material at the end of the seed rod. The growth continues, the crystal growing at the seed rod while the feed rod gets shorter and its composition changes.

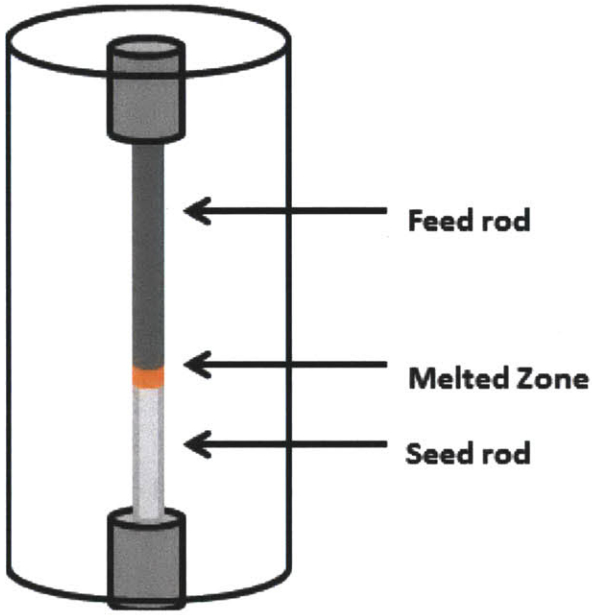

Figure 4-3: Diagram of the floating zone furnace used, radiative heating is used to melt the zone at the focus point(orange). The growth is done in vacuum.

Two problems were encountered when using this method: as the rods started melting in the floating zone, fumes appeared indicating that part of the material was disappearing effectively changing the composition of the molten solid, and as the temperature in the feed rod increased, In in the rod melted and the rod collapsed. Due to these problems it was impossible to get a crystal using the floating zone furnace. A solution to the above-mentioned problems is proposed in Section 4.4, by using a three zone furnace for the growth.

4.4 Three zone furnace

In a three zone furnace, the sample is encapsulated in a quartz tube and placed inside a quartz cylinder. Three heating coils cover the outside of the cylinder as shown in Figure 4-4. By adjusting the current in the three coils it is possible to adjust the gradient of temperature along the direction of the tube, and when cooling down, the material crystallizes following the direction of the gradient.

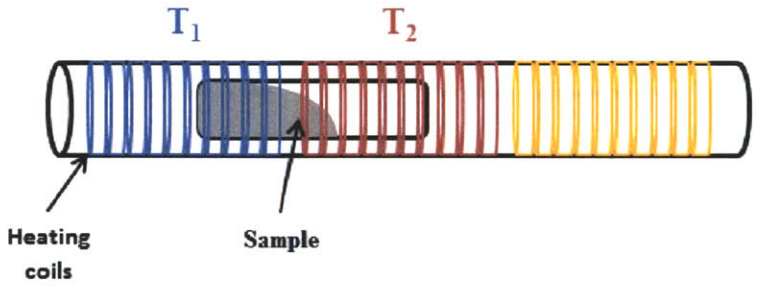

Figure 4-4: Diagram of the three zone furnace used. Three coils are used to create a horizontal temperature gradient. Thermocouples located at the center of each coil are attached to controllers to set the temperature.

The tube is prepared with 0.5g of stoichiometric powder to be used as a seed and 4g of 33% composition powder obtained as described in 4.2. For this experiment only two zones are used: the hot end at temperature T_2 and the cold end at temperature T_1. The stoichiometric powder is placed at the cold end. The temperature is set such that $T_m > T_2 = 540°\text{C} > T_1 = 530°\text{C} > T_{33}$ for a day and then the T_1 and T_2 are both reduced at a rate $r = -10°\text{C/hr}$.

By this method, single crystals were obtained with sizes up to 0.5g. The limitation of this technique is that due to the horizontal position of the samples the material is spread over the whole length of the tube, which is limited by the ability to seal the tube as close as possible to the material without melting it. In Section 4.5 a method is described to obtain a vertically positioned tube with a vertical gradient.

4.5 Bridgman growth using a box furnace

The box furnace shown in Figure 4-2 is modified to accommodate a vertical gradient of temperature. The top of the furnace has an orifice that can be used to add an external thermometer to the furnace. In this setup the orifice is left open to insert a tube held by a three-fingered clamp as shown in Figure 4-5. The sample rest between a hot region inside the furnace, and a cold region outside the furnace. Two methods are used: the temperature is fixed and the tube is pulled up by adjusting the clamp, or the position of the tube is fixed and the temperature of the furnace is changed.

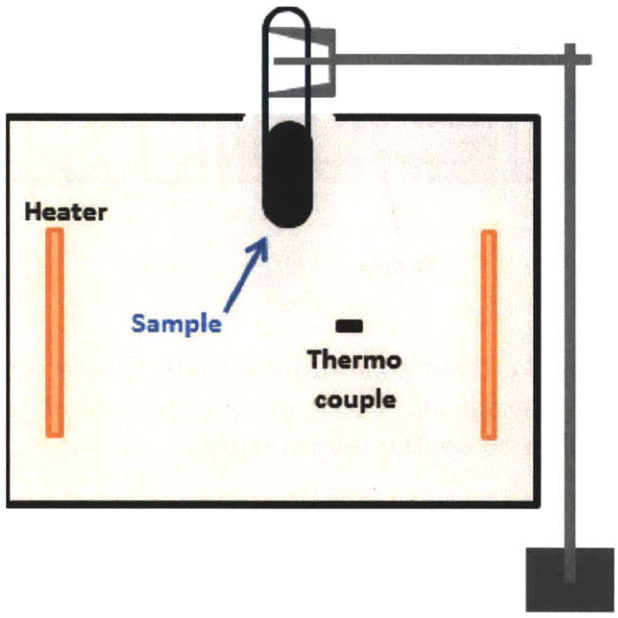

Figure 4-5: Front view diagram of the box furnace used for Bridgman growth. The furnace is open on top where a sample is held in place by a three-fingered clamp.

The samples are prepared by sealing in a quartz tube 33% composition powder topped with a seed, which is either powder as described before or crystalline from previous growths. For the fixed-temperature method the temperature is set to 540°C for a few days before pulling the tube at a rate of 0.5cm/hr. For the fixed-position method the temperature is initially set to 540°C for a few days and then decreased with a rate $r = -0.1$°C/min. The fixed-temperature method proved ineffective since the adjustments in position were done manually, and in the process the contents of the tube were disturbed. With the fixed-position method it was possible to grow

single crystals up to 1.1g. A picture of a typical crystal grown by this method is shown in Figure 4-6.

Figure 4-6: Picture of a large In_4Se_3 crystal. Because the most easily cleavable, the $(1, 0, 0)$ faces are seen in the plane of the picture.

Two crystals were chosen to do neutron scattering on, the first from the three zone furnace growth with a mass of $m_1 = 0.47$g and the second one from the growth using the box furnace with a vertical gradient with a mass $m_2 = 1.1$g.

Chapter 5

Diffraction of waves by crystals

In order to understand the x-ray diffraction and neutron scattering experiments, as well as the structure factor calculations, an introduction to wave diffraction by crystals is required. This chapter presents the theory of diffraction of waves by crystals. The notation here follows [10]; refer to this textbook for a more in-depth derivation.

5.1 Bragg law

Crystalline solids are studied by the means of diffraction of electrons, neutrons and photons to find out the crystal structure, mechanical and magnetic properties. Waves with wavelength much greater than the interatomic spacing incident on a solid, follow optical reflection and refraction relations. When the wavelength is of the same order as the interatomic spacing in the solid, diffraction must be considered.

Consider two rays incident on parallel reflecting planes as depicted in Figure 5-1. The condition for constructive interference is that the difference in path length for the two rays must be an integer number of wavelengths and is known as the Bragg law

$$2d\sin\theta = n\lambda, \tag{5.1}$$

where d is the distance between planes, θ is the angle of incidence, λ is the wavelength of the incident radiation and n is an integer. The law of reflection states that the angle

between the incident ray and the plane of reflection is the same as the angle between the plane of reflection and the reflected ray. So the angle between the incident and reflected rays is 2θ and is usually the one used in crystallography for reasons that will become apparent later.

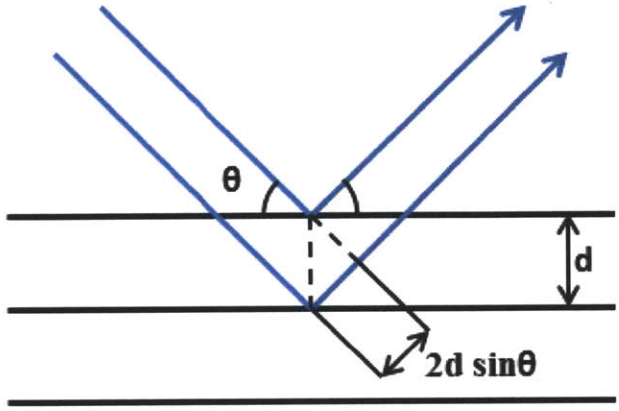

Figure 5-1: By geometrical construction, two rays incident on parallel atomic planes have path length difference $2d \sin\theta$.

5.2 Reciprocal lattice

Photons interact mainly with the electron cloud of solids whereas neutrons interact mainly with the nuclei, and electrons with both. In this section the electron density $n(\mathbf{r})$ is considered to be the only the mechanism for scattering, but the argument can be extended to neutron or electron scattering. Consider a crystal with lattice vector $\mathbf{a_1}$, $\mathbf{a_2}$ and $\mathbf{a_3}$, so that it is invariant under translations $\mathbf{T} = v_1\mathbf{a_1} + v_2\mathbf{a_2} + v_3\mathbf{a_3}$ which are linear combinations of these vectors. Then electron density is periodic $n(\mathbf{r}) = n(\mathbf{r} + \mathbf{T})$, and the Fourier transform is given by

$$n(\mathbf{r}) = \sum_{\mathbf{G}} n_G \exp(i\mathbf{G} \cdot \mathbf{r}), \tag{5.2}$$

and the inverse

$$n_G = \frac{1}{V_c} \int_{cell} n(\mathbf{r}) \exp(-i\mathbf{G} \cdot \mathbf{r}) \mathrm{d}V, \tag{5.3}$$

where V_c is the volume of the unit cell. Through Fourier transforming, the crystal lattice is mapped to a reciprocal lattice, i.e. a lattice in momentum space, such that $\mathbf{G}$ gives the allowed points in momentum that satify the periodicity of $\mathbf{T}$. Defining reciprocal lattice vectors $\mathbf{b_1} = 2\pi\frac{\mathbf{a_2}\times\mathbf{a_3}}{\mathbf{a_1}\cdot\mathbf{a_2}\times\mathbf{a_3}}$, $\mathbf{b_2} = 2\pi\frac{\mathbf{a_3}\times\mathbf{a_1}}{\mathbf{a_1}\cdot\mathbf{a_2}\times\mathbf{a_3}}$, $\mathbf{b_3} = 2\pi\frac{\mathbf{a_1}\times\mathbf{a_2}}{\mathbf{a_1}\cdot\mathbf{a_2}\times\mathbf{a_3}}$, then $\mathbf{G}$ can be written as $\mathbf{G} = u_1\mathbf{b_1} + u_2\mathbf{b_2} + u_3\mathbf{b_3}$ where u_1, u_2, and u_3 are integers. With this $\exp(i\mathbf{G}\cdot\mathbf{T}) = \exp[2\pi i(u_1v_1 + u_2v_2 + u_3v_3)] = 1$ so that the invariance under translation $\mathbf{T}$ is assured.

5.3 Diffraction condition for a crystal

Suppose a wave with wave vector $\mathbf{k}$ is incident on two differential volumes separated by a distance $\mathbf{r}$, and the outgoing wave vector is $\mathbf{k}'$. The angle between $\mathbf{k}$ and $\mathbf{k}'$ is denoted 2θ as in Section 5.1. For the incident wave, the difference in path length between the two points is $r\sin\theta$, so the phase difference is $2\pi r\sin\theta/\lambda = \mathbf{k}\cdot\mathbf{r}$. In a similar manner the phase difference coming from the diffracted portion is $-\mathbf{k}'\cdot\mathbf{r}$. Therefore the phase factor can be written as $\exp[i(\mathbf{k}-\mathbf{k}')\cdot\mathbf{r}]$. Assume that the amplitude of the scattered wave from the differential volume is proportional to the electron density. The total amplitude is then given by the integral

$$F = \int_{crystal} n(\mathbf{r})\exp(-i\Delta\mathbf{k}\cdot\mathbf{r})\,dV, \tag{5.4}$$

where F is called the scattering amplitude, and $\Delta\mathbf{k} = \mathbf{k}' - \mathbf{k}$ is called the scattering vector. Note that the intensity is given by F^*F, so it is fine to have a complex scattering amplitude. Using equation 5.2, equation 5.4 can be written as

$$F = \sum_{\mathbf{G}}\int_{crystal} n_G\exp[i(\mathbf{G}-\Delta\mathbf{k})\cdot\mathbf{r}]\,dV. \tag{5.5}$$

For any $\Delta\mathbf{k} \neq \mathbf{G}$, F is negligible and for $\Delta\mathbf{k} = \mathbf{G}$, the exponential becomes 1 and $F = Vn_G$. Therefore $\mathbf{k}' = \mathbf{k} + \mathbf{G}$ is the Bragg diffraction condition for crystalline solids.

In the case where elastic scattering is considered, the energy of the incident particle is conserved, so $|\mathbf{k}| = |\mathbf{k}'|$ and the condition becomes

$$2\mathbf{k} \cdot \mathbf{G} = G^2. \tag{5.6}$$

5.4 Structure factor

If the diffraction condition is met, the scattering amplitude for a crystal of N cells reduces to

$$F_G = N \int_{cell} n(\mathbf{r}) \exp(-i\mathbf{G} \cdot \mathbf{r}) \mathrm{d}V = NS_G, \tag{5.7}$$

where S_G is called the structure factor, and $\mathbf{r}$ can be chosen to be zero at one corner of the cell. Suppose the cell contains s atoms that contribute to the electron density at $\mathbf{r}$ such that $n(\mathbf{r}) = \sum_{j=1}^{s} n_j(\mathbf{r} - \mathbf{r_j})$ where n_j is the contribution of the jth atom located at $\mathbf{r_j}$. Then the structure factor is given by

$$S_G = \sum_j f_j \exp(-i\mathbf{G} \cdot \mathbf{r_j}), \tag{5.8}$$

and f_j the atomic form factor is

$$f_j = \int n_j(\mathbf{r_0}) \exp(-i\mathbf{G} \cdot \mathbf{r_0}) \mathrm{d}V, \tag{5.9}$$

where $\mathbf{r_0} = \mathbf{r} - \mathbf{r_j}$. f_j is an atomic property and depends on the type of scattering experiment considered. For x-rays, the form factor is not very sensitive to small redistributions of the electrons in comparison to a free atom, and thus it is close to the form factor for electrons localized at the atom, giving the simple form $f_j = Z$ where Z is the atomic number.

With this theoretical prelude, the description of the x-ray diffraction experiments is possible and will be the subject of Chapter 6.

Chapter 6

X-ray diffraction of In_4Se_3

X-ray diffraction experiments can be used to determine the different phases present in a sample, and in the case of single crystals it can be used to determine the orientation of the crystal.

6.1 X-ray powder diffraction

To determine the phases in a sample, x-ray powder is analyzed using a diffractometer. A schematic of the PANalytical X'Pert Pro Multipurpose Diffractometer used for this experiment, is shown in Figure 6-1. Cu K-α x-rays with wavelength $\lambda = 1.54059\mathring{A}$ are produced in the x-ray tube. The beam is collimated and reduced in size using a soller slit collimator, a mask and a fixed divergence slit. The collimated beam is diffracted by the sample and goes through a Ni filter and a soller slit collimator before entering the detector.

6.1.1 Phase identification

The Bragg condition as stated in equation 5.6 on page 36 is met for horizontal planes of reflection at a certain angle 2θ. For a powder there are a huge number of crystallites with random orientations, thus a scan of all possible angles 2θ gives all of the Bragg peaks for the different phases in the solid. The structure factor calculation for In_4Se_3

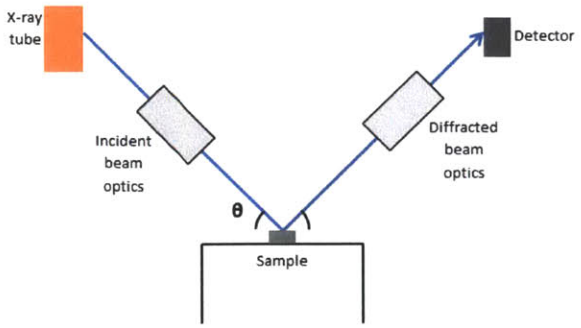

Figure 6-1: Schematic of a multipurpose diffractometer. The incident beam optics include a soller slit collimator, a beam mask, and a fixed divergence slit. The diffracted beam optics include a Ni filter and a soller slit. Cu K-α emission is used.

was performed starting from equation 5.8, using $f_{In} = Z_{In} = 49$ and $f_{Se} = Z_{Se} = 34$, and using the positions specified in Table A.1 in the Appendix A and gives the angles at which Bragg peaks should be present for the In_4Se_3 phase. The MATLAB[11] code can be found in Section B.1 of Appendix B. By comparing the experimental data to the calculated angles corresponding to Bragg peaks, the phase of the solid can be identified. Figure 6-2 shows such comparison, the difference in intensities of the peaks particularly at high angles is due to instrumental factors.

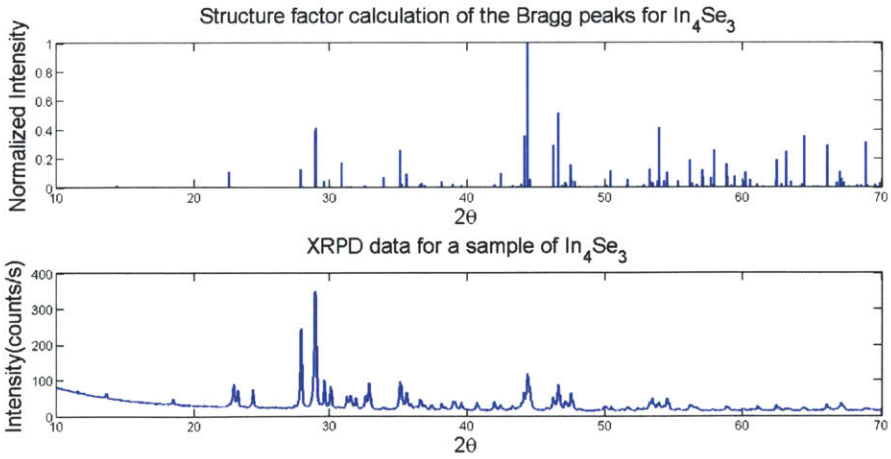

Figure 6-2: Comparison of the structure factor calculations to x-ray diffraction data.

In practice, phase identification is done using software that matches the diffraction pattern with standard patterns in its database for different phases; for this experiment High Score Plus[12] is used.

6.1.2 Phase quantization

A second stage involves determining the quantity of each phase present. This is achieved by looking at the relative intensities of Bragg peaks for the different phases, and can be done with varying levels of accuracy. See [13] for an outline of the different methods. The method of choice is the normalized reference intensity ratio (RIR) method again using High Score Plus. This method allows for a semi-quantitative analysis without having to combine the sample with standards, and without requiring computation power, unlike Rietveld refinement. Preliminary steps include: fitting and removing the background, excluding K-α2 peaks, profile fitting and peak decomposition.

Figure 6-3 is an example of phase quantization done for a sample with multiple phases, primarily InSe. This sample was obtained with the growth method described in 4.1.

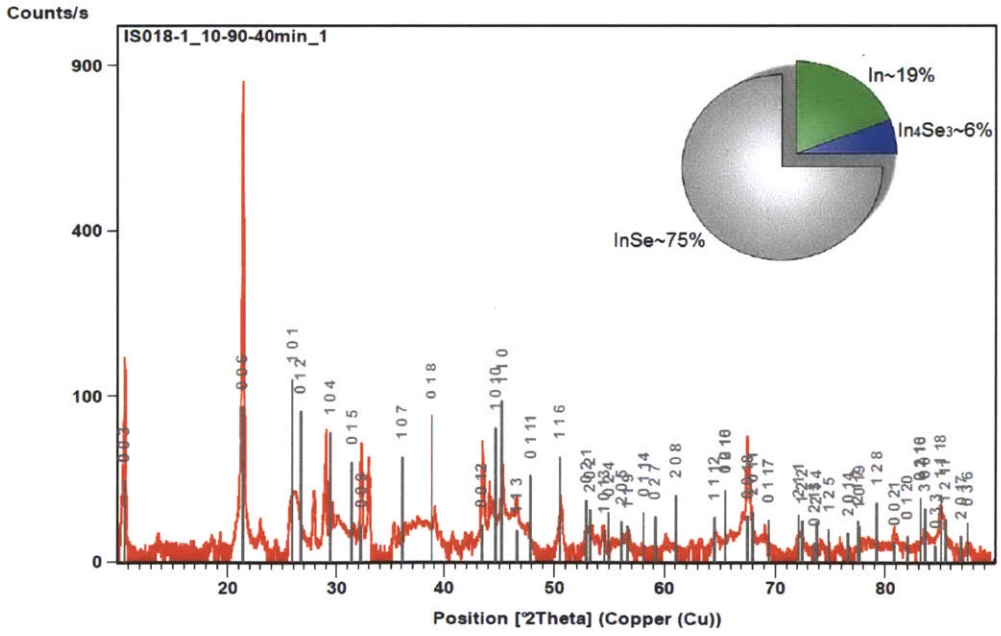

Figure 6-3: Phase quantization for a multiphase sample. The x-ray spectrum is shown in red, peaks associated with InSe in gray. Pie diagram presents the results of a normalized RIR quantization.

6.2 X-ray single crystal diffraction

X-ray diffraction can also be used in a single crystal to determine its orientation. This is particularly useful when preparing for neutron scattering or high resolution x-ray scattering experiments. As mentioned before the setup of the multipurpose diffractometer is such that only horizontal planes of reflection can meet the Bragg condition. Therefore the single crystal must be aligned such that the plane of interest is horizontal. Without a goniometer, this is done by finding two parallel faces in the crystal since these are usually crystallographic planes. In In_4Se_3 the most easily cleavable direction is along a, since the bonds are weaker in this direction as explained in Chapter 3. The crystals show sharp planes only along one direction, and this can be seen in Figure 4-6. Peaks at angles corresponding to $(h, 0, 0)$ are expected. Nevertheless the space group of In_4Se_3 dictates that peaks with $h + k + l =$ odd are forbidden and the structure factor calculation backs this up, thus only $(2n, 0, 0)$ peaks are expected, with $n \in \mathbb{Z}$. Figure 6-4 shows the x-ray pattern obtained with proper alignment.

With one direction determined, the other two are easily obtained when aligning the crystal in the spectrometer at the neutron facility.

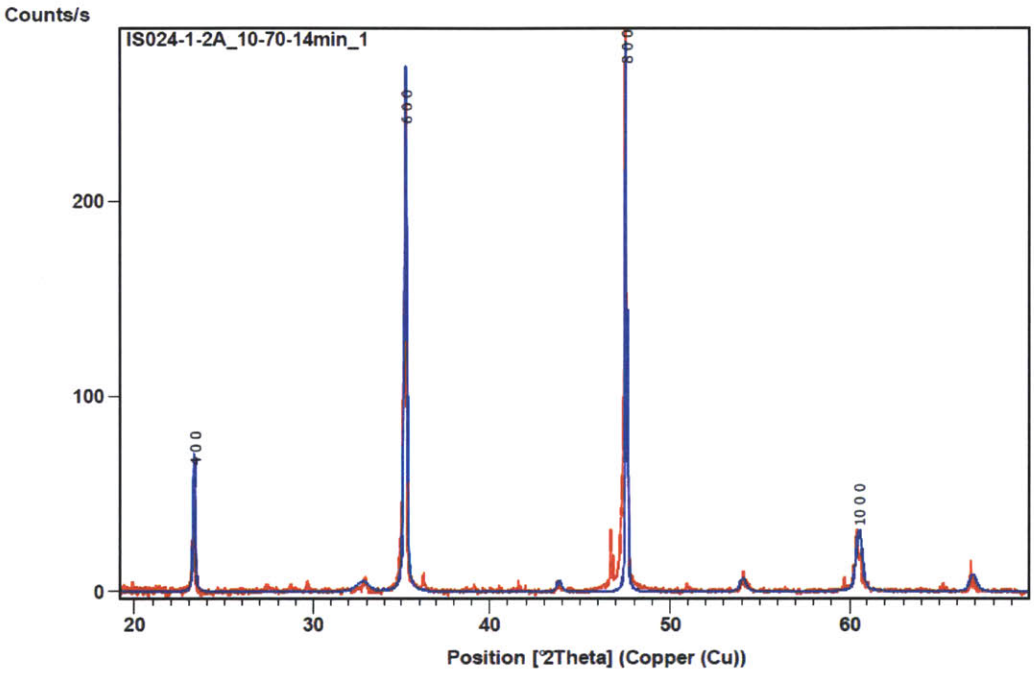

Figure 6-4: Single crystal diffraction of the a face of In_4Se_3 . The x-ray spectrum is shown in red, a peak profile for determination of the position of the peaks is shown in blue. Labels for $(2n, 0, 0)$ peaks are shown in black. Note that the secondary peaks near the Bragg peaks come from the geometry of the crystal having a step, such that x-rays hit a faces at two different distances.

Chapter 7

Neutron Scattering

This chapter focuses on the neutron scattering experiment carried out to explore the structure of the $In_4Se_{3-\delta}$ crystals. Neutron scattering is a powerful technique for analyzing the structure of condensed matter. Being neutral particles, neutrons can penetrate deeply into the sample, and unlike x-rays they do not interact with electron clouds. Therefore the cross section for interaction does not increase with atomic number. Moreover magnetic structure determination is possible since they interact with internal magnetic fields[14]. For neutron scattering the atomic form factor in the scattering amplitude is proportional to the neutron cross section for scattering for the specific atom.

7.1 Neutron absorption

Neutrons can interact with a crystalline sample in two ways: they can scatter with the nuclei following the diffraction conditions introduced in Chapter 5, or they can be absorbed by the nuclei in a nuclear reaction.

Indium is a strong absorber: it has high neutron capture cross section of 193.8 barns for thermal neutrons[15]. The absorption is considered in structure factor calculations by adding an imaginary term to the neutron cross section.

The most common absorption process is described by the absorption of a neutron

followed by a beta decay as stated in the following set of equations

$$ {}^{1}_{0}\mathrm{n} + {}^{115}_{49}\mathrm{In} \rightarrow {}^{116}_{49}\mathrm{In}\,. \tag{7.1a} $$

$$ {}^{116}_{49}\mathrm{In} \rightarrow {}^{116}_{50}\mathrm{Sn} + \mathrm{e}^{-} + \bar{\nu}_{e}\,. \tag{7.1b} $$

Due to the absorption processes, the intensity is reduced, making the features to explore difficult to resolve.

7.2 Experimental setup

The experiment described in this chapter was carried out in the High Flux Isotope Reactor at the Oakridge National Laboratory. The instrument used is the Fixed-Incident-Energy Triple-Axis Spectrometer (HB-1A). The instrument specifications are listed in Table A.2 in the Appendix A. A diagram of the instrument is shown in Figure 7-1.

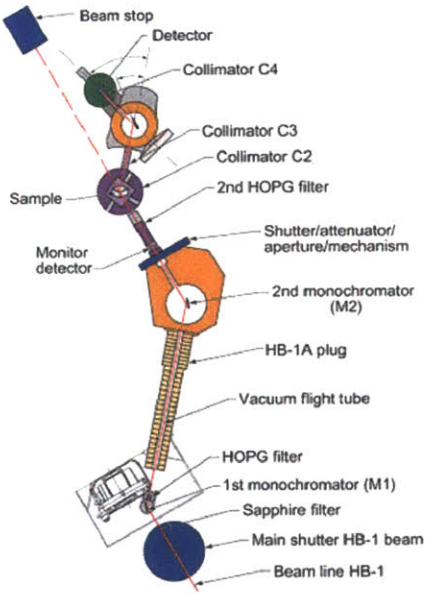

Figure 7-1: Schematic of the Fixed-Incident-Energy Triple-Axis Spectrometer (HB-1A). Adapted from [16].

Neutrons coming out from the beam line HB-1 are filtered, then using two monochromators only neutrons with the appropriate incident energy $E_{incident} = 14.64\mathrm{meV}$ are

allowed. The neutrons are scattered by the sample, collimated and finally reflected to the detector. The scattered energy can be adjusted by changing the reflection angle. A furnace can be incorporated to heat the sample to higher temperatures. The samples are attached to an aluminum holder and then mounted to the goniometer. The alignment is done using the previously determined orientation. The a face is set horizontally such that scattering comes from the b-c plane. Then the peaks at $(0, 4, 0)$ and $(0, 0, 2)$ are found and the angle offsets are set to optimize intensity at these locations.

7.3 Elastic scattering

One of the main objectives of the neutron scattering experiment was to characterize the superlattice structure of $In_4Se_{3-\delta}$. In order to look for superlattice peaks, elastic scattering around intense Bragg peaks is used since the intensity of the superlattice peaks is a lot smaller and roughly proportional to the intensity of the associated Bragg peak.

Scans were done around the proposed $(h, k, l)+(0, 1/2, 1/16)$ and then meshes near intense Bragg peaks were taken. Unfortunately no superlattice peaks were resolved at the positions indicated. Nevertheless, two interesting features were noted.

The first one is a non-zero intensity coming from forbidden Bragg peaks $(0, 0, 1)$ and $(0, 5, 0)$. These two peaks should have zero intensity given that $h + k + l =$ odd. Another PG filter was used to check whether the peaks in question came from neutrons having $\lambda/2$, but the intensity of the peaks did not change significantly proving that the peaks were real. An explanation for this anomaly is that the presence of Se vacancies would give rise to non-zero intensity of these peaks. Simulations are done in Chapter 8 to study this. Figure 7-2 shows a scan at fixed h and l, and varying k around the $(0, 5, 0)$ peak.

The second feature is that the intensity from Bragg peaks (h, k, l) is different to that from $(\bar{h}, \bar{k}, \bar{l})$. The scattering intensity is the norm squared of the scattering amplitude, $I = F^*F$. As long as the form factors f_j is real or the crystal is central-

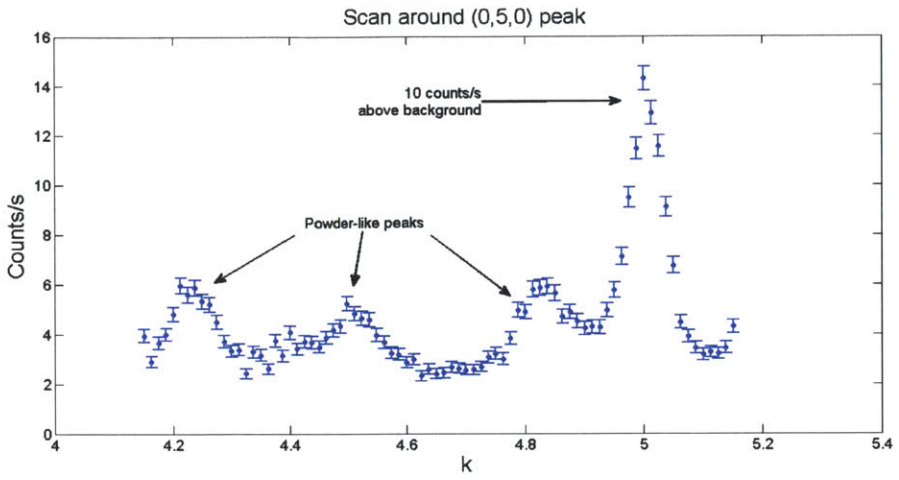

Figure 7-2: Scan in k around the forbidden $(0, 5, 0)$ peak.

symmetric, the intensity from (h, k, l) is the same as the intensity from $(\bar{h}, \bar{k}, \bar{l})$. Indium has an imaginary part to the scattering cross section which corresponds to the absorption, and non central-symmetry could be achieved by having regions of the crystal with a higher selenium vacancy concentration. However geometric factors are difficult to rule out. Figure 7-3 shows a comparison between the intensity of the $(0, 0, 2)$ and $(0, 0, \bar{2})$ peaks.

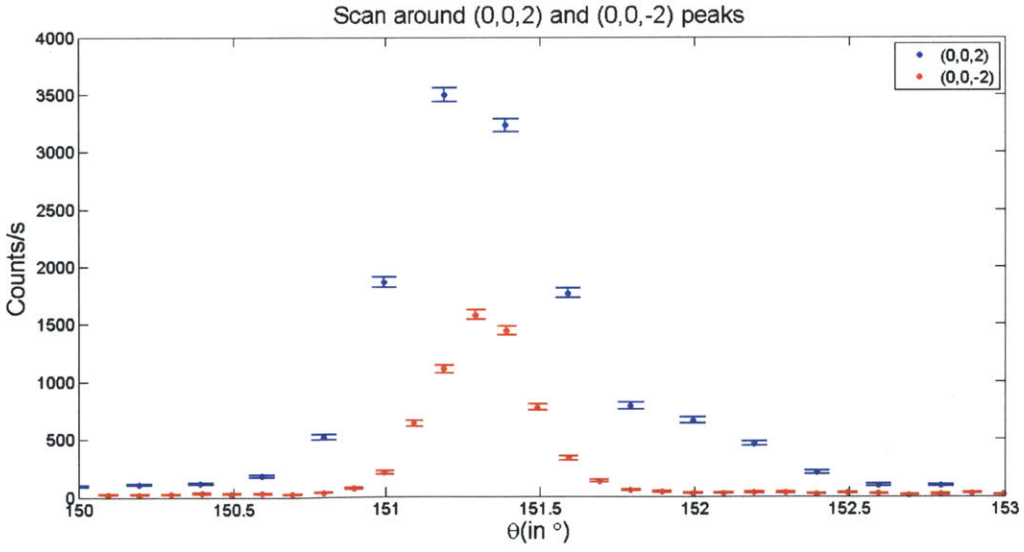

Figure 7-3: Comparison of intensities between $(0, 0, 2)$ and $(0, 0, \bar{2})$ peaks. The position of the $(0, 0, 2)$ peak was shifted 180° to be matched.

7.4 Phonons and inelastic scattering

The second objective of the neutron scattering experiment was to characterize the phonon dispersion for $In_4Se_{3-\delta}$. During inelastic scattering the Bragg condition is obtained for neutrons whose energy changes in the process. This is mediated by phonons in the sample. If the incident energy of the neutron is higher than the scattered energy then a phonon in the crystal was created using the excess energy. Alternatively if the incident energy is lower than the outgoing energy then a phonon present in the crystal was annihilated to give up its energy.

Phonons are collective excitations of the crystal lattice, the energy is related to the frequency of the exited mode by $\epsilon = \left(n + \frac{1}{2}\right)\hbar\omega$ where n is the number of phonons in that mode. In Chapter 5, the condition for scattering $\mathbf{k}' = \mathbf{k} + \mathbf{G}$ was derived. It can be rewritten to account for the creation or annihilation of a phonon with wavevector $\mathbf{K}$ as:

$$\mathbf{k}' \pm \mathbf{K} = \mathbf{k} + \mathbf{G}, \tag{7.2}$$

where the $(+)$ denotes creation and the $(-)$ annihilation. The relation between the magnitude of the wavevector $K = |\mathbf{K}|$ and the frequency ω is non-trivial for phonons. It is called the dispersion relation and accounts for many of the thermal properties of a material as explained in [10]. For a crystal with N unit cells and p atoms per unit cell, there are $3pN$ normal modes of vibration, $3N$ of them are acoustic modes that follow a linear relation for small K, and the other $3N(p-1)$ are called optical phonons where $\frac{\mathrm{d}\omega}{\mathrm{d}K} = 0$ at $K = 0$. For both acoustic and optical phonons, $\frac{\mathrm{d}\omega}{\mathrm{d}K} = 0$ at the Brillouin zone boundary which is when $\mathbf{K}$ is half way between two reciprocal lattice points. Additionally there can be three polarizations for phonons: one longitudinal when the vibration is in the same direction as the direction of propagation, and two transversal when it is perpendicular.

In this experiment we wanted to trace some of the phonon dispersion curves. To do this, scans were taken at specific locations near reciprocal lattice points while varying the scattered energy. If a peak in energy is identified at this position, as the

position is increased the energy should follow the dispersion relation, given that it is proportional to frequency.

Unfortunately no peaks corresponding to phonons were resolved during the experiment. The temperature was increased to 600K in hopes of increasing the intensity. Since the phonons in a solid follow Maxwell-Boltzmann distribution at high temperatures, then the higher the temperature the higher the number of phonons of any given energy, so the more likely a phonon will annihilate to transfer its energy to the neutron. Still no phonons were identified.

Due to the high neutron absorption of indium, no superlattice peaks and no phonons were resolved. A natural next step to the project would be to investigate the structure of $In_4Se_{3-\delta}$ crystals using high resolution x-ray scattering.

Chapter 8

Effect of Se vacancies on Bragg intensities of $In_4Se_{3-\delta}$

The non-zero intensity of forbidden peaks discovered in the neutron experiment described in Chapter 7 could be due to the selenium vacancies present in the lattice. To explore the effects of the vacancies on the intensities of the Bragg peaks, two approaches are taken to calculate the scattering amplitude. The first approach is to consider an analytical solution to the simple case of a 1-D lattice with one atom per lattice site, and remove atoms at random. This approach gives a qualitative description. The second approach is to use simulations with an In_4Se_3 lattice with 10^6 cells ($100 \times 100 \times 100$), where selenium atoms are removed at random, to get a quantitative result. The assumption that the absence of a selenium atom in a given site does not affect the absence of a selenium atom in any other site is made. This assumption is valid as long as δ is small.

8.1 1-D analytical solution for forbidden peaks

The simple case of a 1-D lattice where some of the atoms are missing is considered. Assume that there is only one atom per lattice site and that the lattice constant is l_0. For a perfect crystal, consider the direction G_0 corresponding to a forbidden peak, the scattering intensity is 0 thus the scattering amplitude is as well. Now take the

case of a crystal with vacancies

$$\begin{aligned} F_{G_0} &= \sum_{\text{atoms present } j} f \exp\left(-iG_0 x_j\right) \\ &= \sum_{\text{All lattice points } j} f \exp\left(-iG_0 x_j\right) - \sum_{\text{atoms absent } j} f \exp\left(-iG_0 x_j\right), \end{aligned} \tag{8.1}$$

where f is the atomic form factor for the given atom and x_j is the position of the jth atom. The first term in the sum is 0 as explained before, and the second term corresponds to a Poisson process for the distance between vacancies assuming p (the probability of missing an atom) is small and the crystal is infinite. $x_j = \sum_{s=1}^{j} x^{(s)}$, where $x^{(s)}$ are the independent variables in the Poisson process. In this case the expectation value can be evaluated so that equation 8.1 becomes

$$F_{G_0} = -f \left\langle \sum_{j=1}^{\infty} \exp\left(-iG_0 \sum_{s=1}^{j} x^{(s)}\right) \right\rangle. \tag{8.2}$$

The expectation value of a sum is the sum of the expectation values

$$F_{G_0} = -f \sum_{j=1}^{\infty} \left\langle \exp\left(-iG_0 \sum_{s=1}^{j} x^{(s)}\right) \right\rangle \tag{8.3}$$

Since the $x^{(s)}$ are considered independent variables

$$\begin{aligned} F_{G_0} &= -f \sum_{j=1}^{\infty} \prod_{s=1}^{j} \left\langle \exp\left(-iG_0 x^{(s)}\right) \right\rangle \\ &= -f \sum_{j=1}^{\infty} \left\langle \exp\left(-iG_0 x^{(s)}\right) \right\rangle^{j}. \end{aligned} \tag{8.4}$$

To calculate this quantity the specific probability distribution is needed. The probability of finding exactly one atom at a distance $x = l_0 u$ is the probability of not finding an atom between 0 and $l_0(u-1)$ times the probability of finding one at $l_0 u$. Here u is an integer.

$$P(u) = \text{Poisson}(0, p(u-1))\text{Poisson}(1, p) = p \exp\left(-pu\right). \tag{8.5}$$

where $\text{Poisson}(k,\lambda) = \frac{\lambda^k \exp(-\lambda)}{k!}$ is the Poisson distribution. It follows from this result after normalization, that

$$\left\langle \exp\left(-iG_0 x^{(s)}\right)\right\rangle = \frac{\exp\left(iG_0 l_0\right)\left[\exp\left(p\right)-1\right]}{\exp\left(iG_0 l_0 + p\right) - 1}. \tag{8.6}$$

Therefore,

$$\begin{aligned} F_{G_0} &= -f\frac{\exp\left(iG_0 l_0\right)\left[\exp\left(p\right)-1\right]}{\exp\left(iG_0 l_0\right)-1} \\ I_{G_0} &= F^*_{G_0} F_{G_0} \\ &= f^2 \frac{\left[\exp\left(p\right)-1\right]^2}{2\left[1-\cos\left(G_0 l_0\right)\right]}. \end{aligned} \tag{8.7}$$

For small p, equation 8.7 gives $I_{G_0} \propto p^2$, a quadratic dependence to first order in p.

8.2 Simulations for a finite $In_4Se_{3-\delta}$ crystal

In Chapter 5, an equation to calculate the scattering amplitude F_G in a given direction $\mathbf{G}$ in a perfect crystal was derived

$$F_G = N\sum_j f_j \exp\left(-i\mathbf{G}\cdot\mathbf{r_j}\right),$$

where f_j is the atomic form factor, and r_j is the position of the jth atom in the unit cell.

For an $In_4Se_{3-\delta}$ crystal, where some of the Se atoms are missing the equation becomes

$$F_G = \sum_{Allcellss}\left(\sum_{j=0}^{16} f_{In}\exp\left[-i\mathbf{G}\cdot\left(\mathbf{r_j}+\mathbf{r_s}\right)\right] + \sum_{j=17}^{28}\theta(p) f_{Se}\exp\left[-i\mathbf{G}\cdot\left(\mathbf{r_j}+\mathbf{r_s}\right)\right]\right), \tag{8.8}$$

where $\theta(p)$ is a random variable that can takes the value 0 with probability p and 1 with probability $1-p$, f_{In} is the atomic form factor for indium, f_{Se} is the atomic

form factor for Se, and $\mathbf{r_s}$ is the position of the sth unit cell. Note that the labels of the atoms in a unit cell are such that the first 16 atoms are the indium and the rest are selenium atoms. For an $In_4Se_{3-\delta}$ crystal $p = \frac{\delta}{3}$.

To determine the size of the crystal to use, a convergence check was executed in which the variation of the intensity of different peaks was studied as N the number of unit cells was increased. For $N = 10^6$, the variations in the relative intensity are in the order of 10^{-4}, so it was deemed appropriate.

The MATLAB code used for the final calculation can be found in Section B.2 in the Appendix B, and the results are presented in Figure 8-1. The intensity of the forbidden peaks has a quadratic dependence on δ as predicted by the solution derived before. A plot of the relative intensity of $(0, 0, 1)$ versus δ^2 is shown in Figure 8-2, and the points are fitted to a line with excellent agreement ($R^2 = 1 - 1 \times 10^{-5}$).

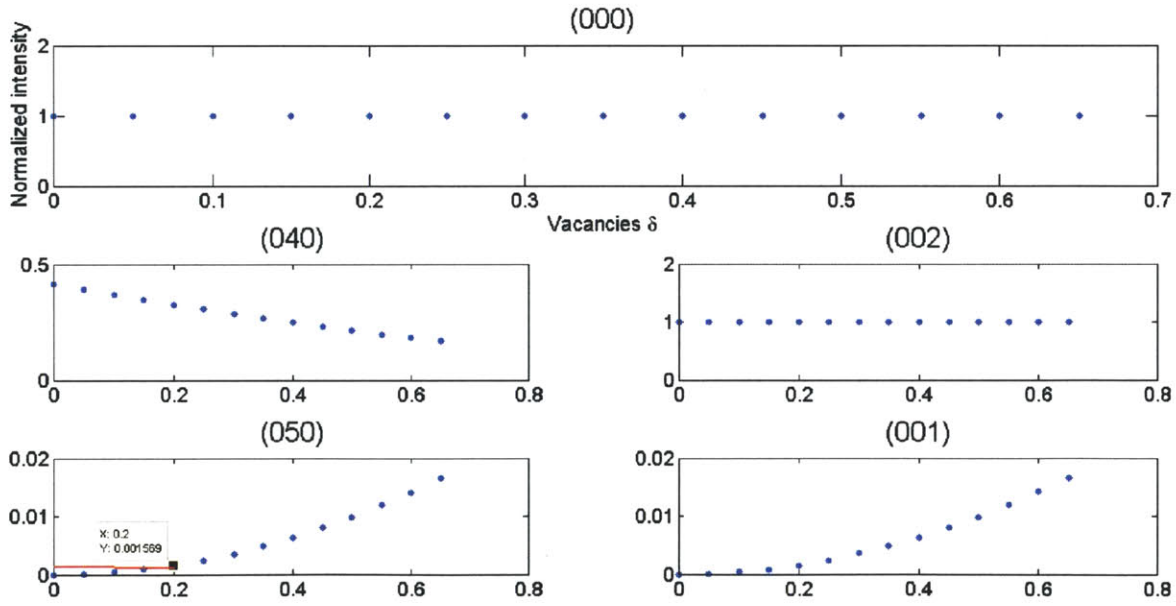

Figure 8-1: Relative intensity of Bragg peaks $(0, 0, 0)$, $(0, 4, 0)$, $(0, 5, 0)$, $(0, 0, 2)$ and $(0, 0, 1)$ as a function of the number of vacancies δ . The intensities are normalized to the intensity of the $(0, 0, 0)$ peak.

The ratios of forbidden peak intensity to the intensity of the adjacent Bragg peak determined in the neutron scattering experiment for one of the crystals, are $\frac{I_{(0,5,0)}}{I_{(0,4,0)}} = 4 \times 10^{-3}$ and $\frac{I_{(0,0,1)}}{I_{(0,0,2)}} = 2 \times 10^{-3}$. From the simulations, this ratio corresponds

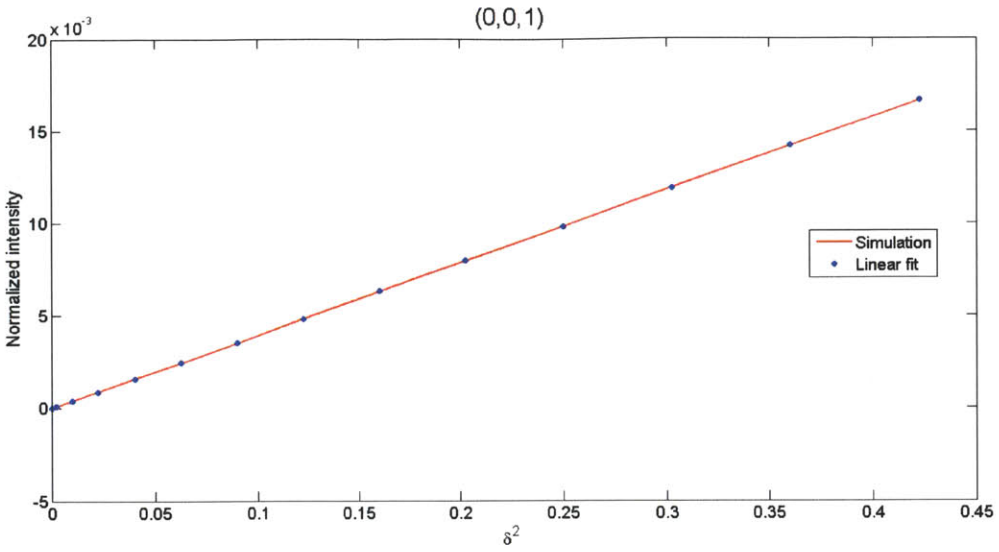

Figure 8-2: Relative intensity of $(0, 0, 1)$ versus δ^2. The red line is a linear fit to the points. The intensity is normalized to the intensity of the $(0, 0, 0)$ peak.

in both cases to a $\delta = 0.2$. The fact that the two results agree is encouraging, but a definite statement cannot be made from two data points.

Chapter 9

Results and conclusions

To evaluate the figure of merit ZT of a thermoelectric crystal, three quantities must be measured as a function of temperature: the electrical resistivity ρ, the Seebeck coefficient S and the thermal conductivity κ. Electrical resistivity and Seebeck coefficient data for one of the $In_4Se_{3-\delta}$ crystals along the b-c plane, were taken by D. Gardner[1] and W. Shu[2] at Prof. Ren's laboratory[3]. A comparison between the thermoelectric measurements taken and those from other groups is presented in Figure 9-1. Ren's sample is a powder, Rhyee published data for a crystalline sample in two directions: in the b-c plane and in the a-c plane[6].

The combined result $\frac{S^2}{\rho}$ for our crystals is in accordance with Ren's powder and Rhyee's a-c measurements, but it is considerably lower than Rhyee's b-c measurement. This is mainly caused by the relatively high electrical resistivity of our sample. Thermal conductivity measurements have not been taken.

To summarize the project on synthesis and physical characterization of thermoelectric single crystals:

1. $In_4Se_{3-\delta}$ is proposed as a good n-type thermoelectric material, due to the presence of a Peierls distortion along the b direction[6].

2. $In_4Se_{3-\delta}$ crystals were grown by different methods including the use of a floating

[1]Massachusetts Institute of Technology
[2]Boston College
[3]Boston College

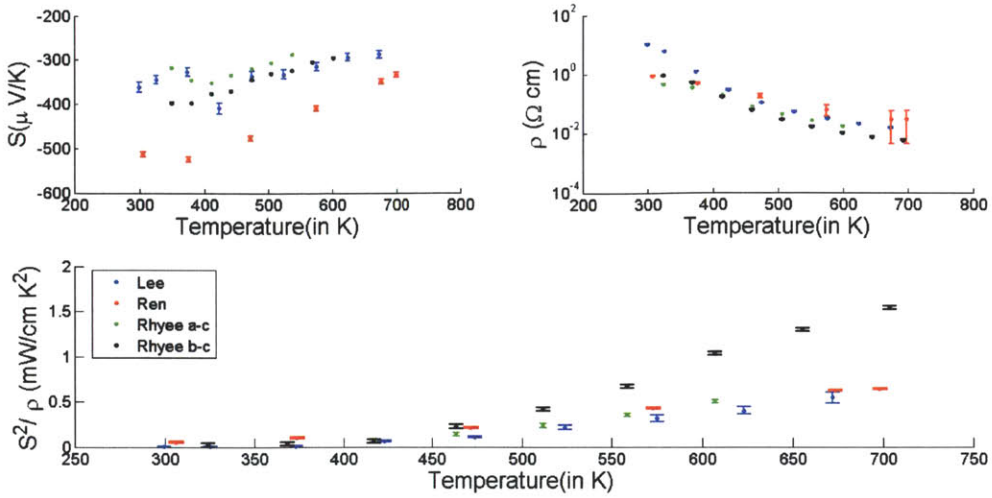

Figure 9-1: Thermoelectric measurements. Restivity ρ, Seebeck coefficient S and $\frac{S^2}{\rho}$ are plotted versus temperature for four different samples.

zone furnace and a three zone furnace along with different initial compositions. It was found that the Bridgman method using an In_4Se_3 seed along with a 33% indium composition melt in the three-zone furnace or in a modified setup of the box furnace was the most reliable.

3. To characterize the phases of each sample, x-ray diffraction was used. The position of Bragg peaks revealed the nature of the phases, while the relative intensity gave an indication of the amount of each phase present. For single crystals, x-ray diffraction was used to find the orientation of the crystal, in preparation for the neutron scattering experiment.

4. The crystals were studied by the means of neutron scattering at Oak Ridge National Laboratory. Two main objectives of the project were to characterize the superlattice structure of $In_4Se_{3-\delta}$ and to trace phonon dispersion curves for the material. Unfortunately, no superlattice peaks nor phonons were resolved. Since indium has a high neutron absorption, small features are difficult to resolve.

5. Two interesting observations were made: a non-zero intensity of forbidden Bragg peaks, and a difference in intensity between (h, k, l) and $(\bar{h}, \bar{k}, \bar{l})$ peaks.

6. The effect of selenium vacancies in the crystal was explored by the use of simulations, and it is shown that the non-zero intensity of forbidden Bragg peaks could be the result of having a $In_4Se_{2.8}$ composition.

7. Thermoelectric measurements were done, and it is found that the thermoelectric properties are comparable to previous results but somewhat lower than the best results available.

The continued study of $In_4Se_{3-\delta}$ crystals by different techniques such as high resolution x-ray diffraction, or electron diffraction techniques will further the understanding of the underlying nature of this material.

Appendix A

Tables

Table A.1: Position of atoms in In_4Se_3 unit cell specified using the lattice coordinate system.

Index	Atom	Coordinates		
1	In1	0.71105	0.33933	0.00000
2	In1	0.28895	0.66067	0.00000
3	In1	0.21105	0.16067	0.50000
4	In1	0.78895	0.83933	0.50000
5	In2	0.81578	0.52362	0.00000
6	In2	0.18422	0.47638	0.00000
7	In2	0.31578	0.97638	0.50000
8	In2	0.68422	0.02362	0.50000
9	In3	0.96733	0.64423	0.00000
10	In3	0.03267	0.35577	0.00000
11	In3	0.46733	0.85577	0.50000
12	In3	0.53267	0.14423	0.50000
13	In4	0.42369	0.39749	0.00000
14	In4	0.57631	0.60251	0.00000
15	In4	0.92369	0.10251	0.50000

Continued on Next Page...

Table A.1 – Continued

Index	**Atom**	**Coordinates**		
16	In4	0.07631	0.89749	0.50000
17	Se1	0.90329	0.84943	0.00000
18	Se1	0.09671	0.15057	0.00000
19	Se1	0.40329	0.65057	0.50000
20	Se1	0.59671	0.34943	0.50000
21	Se2	0.76875	0.13857	0.00000
22	Se2	0.23125	0.86143	0.00000
23	Se2	0.26875	0.36143	0.50000
24	Se2	0.73125	0.63857	0.50000
25	Se3	0.42410	0.15595	0.00000
26	Se3	0.57590	0.84405	0.00000
27	Se3	0.92410	0.34405	0.50000
28	Se3	0.07590	0.65595	0.50000

Table A.2: Specifications of the Fixed-Incident-Energy Triple-Axis Spectrometer (HB-1A) used for neutron scattering[16].

Beam Spectrum	Thermal
Monochromator	PG(002) double crystal
Monochromator angle	$2\Theta_M = 41.3°$ $E_l = 14.64$meV
Analyzers	PG(002) Be (101) Be(002) Si(111) Ge(111)
Sample angles	$0° < \Psi < 360°$
Scattering angle	$-15° < \Phi < 140°$
Analyzer angles	$-60° < 2\Theta A < 120°$
Collimations	C1: open (48' effective) C2: open (40' effective) (30',20',10') C3: 40', 30', 20', 10' (sample-analyzer) C4: 34', 68', 136' (analyzer-detector)
Beam Size	40×150 mm max
Filters	Sapphire pre-Monochromator-1 HOPG ($\lambda/2 \approx 10^{-4}\lambda$) located between M-1 and M-2 and after M-2
Flux at sample	$\sim 2 \times 10^7$n/cm^{2}s (est.)
Momentum range	0.2 to 4.9$\mathring{A}^{-1}$ (elastic configuration)
Energy transfer	~ -35meV to $+11$meV at $q = 3\mathring{A}^{-1}$

Appendix B

Code

B.1 matlab code for the structure factor calculation of In_4Se_3

```
 clc;clear;close all;
%For neutrons
e=14.6521;%meV
h=4.135668*10^-12;%meV s
c=2.99792458*10^18;%A/s
m=939.565378*10^9/c^2;%meV/c^2
p=sqrt(2*m*e);
lambda=h/p;
Zse = 7.97;
Zin = 4.065;
%For x-rays
Zse=34;
Zin=49;
lambda=1.54059;%in Angstroms, Cu-alpha source
a1=15.296; a2=12.308; a3=4.0806;
a=[a1,a2,a3];
%read position of the atoms
rd=importdata('In4Se3atoms.ATD',' ',9);
```

```
SeV=rd.data(17:28,2:4);
InV=rd.data(1:16,2:4);
hmax=4; kmax=10; lmax=10;
nmax=(hmax+1)*(kmax+1)*(lmax+1);

%Initialize
Res=zeros(nmax,5); count=0;

%all (hkl) between (000) (hmax kmax lmax)
for h=0:hmax
for k=0:kmax
for l=0:lmax
  count=count+1;
  v=[h;k;l];
  [d twoth q]=findDhkl(a,transpose(v),lambda);
  %Structure factor
  Sg=sum(Zse*exp(-2*pi*1i*(SeV*v)))+sum(Zin*exp(-2*pi*1i*(InV*v)));
  %Intensity
  I=abs(Sg)^2;

  %matrix with results
  Res(count,:)=[q h k l I];
end
end
end
Res=sortrows(Res);
%Normalize using the (000) peak
Res(:,5)=Res(:,5)/Res(1,5);

dlmwrite('BraggPeak.csv', Res, '\t');
```

B.2 matlab code for the simulations of selenium vacancies in an $In_4Se_{3-\delta}$ crystal

```
clc;clear;close all;
%For neutrons
e=14.6521;%meV
h=4.135668*10^-12;%meV s
c=2.99792458*10^18;%A/s
m=939.565378*10^9/c^2;%meV/c^2
p=sqrt(2*m*e);
lambda=h/p;
Zse = 7.97;
Zin = 4.065;
%For x-rays
%Zse=34;
%Zin=49;
%lambda=1.54059;%Cu-alpha source
a1=15.296;
a2=12.308;
a3=4.0806;
a=[a1,a2,a3];
%read position of the atoms
rd=importdata('In4Se3atoms.ATD',' ',9);
SeV=rd.data(17:28,2:4);
InV=rd.data(1:16,2:4);
%Bragg peaks to check
arr=[0 0 0;1 0 0;2 0 0;3 0 0;4 0 0;5 0 0;6 0 0;7 0 0;8 0 0];
nmax=length(arr);
[mSe nSe]=size(SeV);
[mIn nIn]=size(InV);
iter=99;%100 unit cells
delta=0:0.05:0.65;%vacancies to check
Res=zeros(nmax,5+length(delta));
%loop through peaks
for ncnt=1:nmax
    v=transpose(arr(ncnt,:));
    [d twoth q]=findDhkl(a,transpose(v),lambda);
    Sg=sum(Zse*exp(-2*pi*1i*(SeV*v)))+sum(Zin*exp(-2*pi*1i*(InV*v)));
    I=abs(Sg)^2;
```

```
    I2=zeros(1,length(delta));
    %loop through probabilities
    for pcnt=1:length(delta)
        pSe=(3-delta(pcnt))/3;
        preF=ones(mSe,1);
        Sg=0;
        icnt=0;
        %loop through crystal
        for m=0:iter
            for n=0:iter
                for o=0:iter
                    icnt=icnt+1;
                    preF(1:mSe)=round(1-0.5/pSe*rand(mSe,1));
                    SeV2=((SeV+m*ones(mSe,1)*[1 0 0]...
        +n*ones(mSe,1)*[0 1 0]+o*ones(mSe,1)*[0 0 1])*v).*preF;
                    InV2=(InV+m*ones(mIn,1)*[1 0 0]...
        +n*ones(mIn,1)*[0 1 0]+o*ones(mIn,1)*[0 0 1])*v;
                    Sg=Sg+sum(Zse*exp(-2*pi*1i*SeV2))...
        +sum(Zin*exp(-2*pi*1i*InV2));
                end
            end
        end
        I2(pcnt)=abs(Sg)^2;
    end
    Res(ncnt,:)=[q v(1) v(2) v(3) I I2];
end
Res=sortrows(Res);
%Normalize
for cnt=5:5+length(delta)
Res(:,cnt)=Res(:,cnt)/Res(1,cnt);
end
```

Bibliography

[1] Thermoelectric effect. In Editors in Chief: Franco Bassani, Gerald L. Liedl, and Peter Wyder, editors, *Encyclopedia of Condensed Matter Physics*, pages 180 – 187. Elsevier, Oxford, 2005.

[2] Francis J. DiSalvo. Thermoelectric cooling and power generation. 285(5428):703–706, 1999.

[3] Thermoelectric and energy conversion devices. In Editors in Chief: Franco Bassani, Gerald L. Liedl, and Peter Wyder, editors, *Encyclopedia of Condensed Matter Physics*, pages 173 – 180. Elsevier, Oxford, 2005.

[4] Hal Edwards, Qian Niu, and Alex de Lozanne. Thermoelectric conversion. In *Wiley Encyclopedia of Electrical and Electronics Engineering*. John Wiley & Sons, Inc., 2001.

[5] V. P. Savchin. *Fiz. Tekh. Poluprovodn.*, 15(1430), 1981.

[6] Jong-Soo Rhyee, Kyu Hyoung Lee, Sang Mock Lee, Eunseog Cho, Sang Il Kim, Eunsung Lee, Yong Seung Kwon, Ji Hoon Shim, and Gabriel Kotliar. Peierls distortion as a route to high thermoelectric performance in In(4)Se(3-delta) crystals. *NATURE*, 459(7249):965–968, JUN 18 2009.

[7] D. M. Bercha, K. Z. Rushchanskii, and M. Sznajder. Phonon spectrum of the layered in4se3 crystal. *physica status solidi (b)*, 212(2):247–261, 1999.

[8] Tadashi C. Ozawa and Sung J. Kang. *Balls&Sticks*: easy-to-use structure visualization and animation program. *Journal of Applied Crystallography*, 37(4):679, Aug 2004.

[9] Li J.B. In-se phase diagram, 2003.

[10] Charles Kittel. *Introduction to Solid State Physics*. John Wiley & Sons, Inc, 2005.

[11] MATLAB. *version 7.13.0.564 (R2010b)*. The MathWorks Inc., Natick, Massachusetts, 2011.

[12] High Score Plus. *version 3.0e*. PANalytical B.V., 2011.

[13] James R. Connolly. Introduction quantitative x-ray diffraction methods, 2012.

[14] R. Pynn. Neutron scattering: A primer. *Los Alamos Science*, 19(19):1–32, 1990.

[15] Varley F. Sears. Neutron scattering lengths and cross sections. *Neutron News*, 3(3):33, 1992.

[16] Fixed-incident-energy triple-axis spectrometer (hb-1a), 2011.